Dynamics of an idealized respiratory-type flow: Tidal exchange across intermediate Reynolds numbers

E. G. Connor, A. C. True, and J. P. Crimaldi[*]

Civil, Environmental, and Architectural Engineering University of Colorado, Boulder, Colorado 80309, USA

Respiratory-type flows facilitate the exchange of fluid through an orifice in many natural and engineered environments. The external flow dynamics for an idealized respiratory-type flow, consisting of periodic inhalation and exhalation of a fixed tidal volume of fluid through a circular orifice at the end of a tube, are investigated. In both numerical and experimental investigations, inertial effects produce asymmetric inhalant and exhalant flow structures, resulting in a dynamic exchange of fluid volume across the orifice. A Lagrangian approach is used to quantify the reinhalation ratio r_I, defined as the amount of exhaled fluid that is subsequently reinhaled. Results show that these flow structure asymmetries and hence r_I are strongly sensitive to Reynolds number, and, to a lesser extent, Womersley number or Strouhal number. At low Reynolds number, where viscous effects dominate, we observe flow kinematics similar to an ideal source or sink and the exchange ratio asymptotes to an upper limit. As the inertial effects become more dominant with increasing Reynolds number, we instead observe jetlike flow structures and a rapid decrease in r_I. In the context of biological sensory and metabolic processes, these results suggest organisms can optimize the exchange of fluid with surrounding environment by modulating the asymmetries in the flow structures arising during olfactory and respiratory activity.

I. INTRODUCTION

Respiratory-type flows feature periodic inhalation and exhalation of a fixed tidal volume of fluid through an orifice. Volume conservation during the inhalant and exhalant phases yields a net-zero (phase-averaged) mass flux. However, with the exception of the highly viscous low-Reynolds limit, asymmetry between inhalant and exhalant flow structures produces a net-positive (outward) momentum flux. This flow asymmetry also produces a dynamic exchange of fluid crossing the orifice; the efficiency of this exchange is of key importance in many engineered and biological systems. In this study, we consider an idealized system that can provide generalizable insights into the fundamental parameters governing the flow and the exchange dynamics of respiratory-type flows.

Diverse examples of respiratory-type flows occur throughout the natural world. Both aquatic and terrestrial animals use respiratory-type flows to sample the environment for metabolic intake or to intercept sensory information [1,2]. Other respiratory-type flow examples are analogous to the processes of respiration and olfaction, in which the lung capacity dictates the tidal volume exchanged through the mouth or nostrils. For example at the geophysical scale, tidal exchange is a respiratory-type flow that facilitates water renewal in estuaries and bays [3–5]. A remarkably similar flow occurs at a smaller scale when honeybees ventilate their hive by actively fanning air in and out

---

[*]crimaldi@colorado.edu

as temperature levels or CO_2 levels rise [6,7]. Respiratory-type flows are also observed as jellyfish periodically expand and contract their bell-shaped bodies for locomotion and feeding [8,9]. While many instances of respiratory-type flows have been examined in depth, previous investigations feature geometries and flow parameters specific to a particular ecological or biological case study.

In many respiratory-type flows, like respiration and sniffing, it is advantageous to minimize reinhalation of previously exhaled fluid. This ensures that waste products (e.g., CO_2) are expelled without reinhalation, and it guarantees that fresh metabolites or samples of odorant information are efficiently obtained with every inhale. In this study, we quantify the ratio of the volume of reinhaled fluid relative to the total volume exchanged during one cycle as the reinhalation ratio r_I. Depending on the dynamics of the flow field, r_I can vary between zero and one, with a smaller value indicating less recycling of the same fluid. Previous biologically and ecologically motivated studies have quantified fluid exchange for specific cases [10,11], but they fail to provide generalizable insight into the variation of r_I due to fundamental governing parameters.

To overcome this from a conceptual standpoint, a simplified approach is sometimes taken while considering respiratory-type flow dynamics in which the inhalant and exhalant phases of the external flow are regarded as independent and are treated separately [3]. In this commonly used framework, it is assumed that a cyclic inhale and exhale occur as a superposition of pure inhalant and exhalant flows with each regime having negligible effect on the other. It is also assumed that as isolated events, inhalant flows are similar to potential sink flows in which fluid is drawn into the orifice omnidirectionally [12,13]. Using an idealized system, True and Crimaldi found that at low Reynolds number (Re), viscous effects cause mass to be drawn into the orifice preferentially from above rather than omnidirectionally [14]. Despite the apparent simplicity of pure inhalant flows, they exhibit surprising dynamics with behaviors that can vary when different system geometry and characteristic flow rate result in varying Re.

Like inhalant flows, some studies focus on exhalant flows exclusive of periodic regimes. When considering them as isolated events, exhalant flows manifest different flow regimes depending on Re. At low Re, exhalant flows are similar to potential source flows. At higher Re, exhalant flows are jetlike and inertial effects dominate viscous effects. Turbulent jets have been studied extensively; among the jet phenomena arising from nonlinear flow dynamics, many studies have focused on vortex formation occurring in the early stages of the jet [15–17]. Vortex ring formation has even been shown partly necessary for jellyfish propulsion which is an example of a respiratory-type flow [8,9].

While periodic respiratory-type flows exhibit characteristics of pure inhalant and exhalant flows, they also display complex dynamics resulting from nonlinear interactions between the two phases of the flow. Studies of synthetic jets (net-zero mass flux) provide important insights into the dynamics of respiratory-type flows featuring periodic inhalation and exhalation [18]. These devices consist of a flat plate with an orifice covering a cavity filled with fluid. A diaphragm on the side of the cavity opposite the orifice is then vibrated at frequencies in the kHz range. In this way, fluid is periodically expelled and entrained into the cavity. The cyclic flow behavior of synthetic jets is fundamentally different from continuous jet flow. Compared with continuous jets, synthetic jets have an enhanced spreading rate [19,20], enhanced mass entrainment [21,22], and earlier transition to turbulence [23]. Synthetic jets offer a useful framework for studying respiratory-type flows, but have been used mainly for flow control in propulsion and airfoil design [20,24–28], or for turbulent mixing applications [29–33]. Consequently, these studies emphasize the addition of momentum to an external flow field by synthetic jets rather than the mass exchange occurring between the device and surrounding fluid.

In this work, we quantify the mass exchange during respiratory-type flows at a range of intermediate Re relevant to biological sensory and metabolic processes. To better isolate the effects of the nondimensional flow parameters, we revisit the geometrically simplified model that was used to study purely inhalant flow cases by True and Crimaldi [14]. As in the previous experiment, our model consists of a cylindrical tube immersed in a large fluid body (Fig. 1), but in the present study fluid is periodically drawn into the tube through a single orifice and expelled through the same orifice. The flow physics of interest to us occur in the fluid environment outside of the tube. Adding a
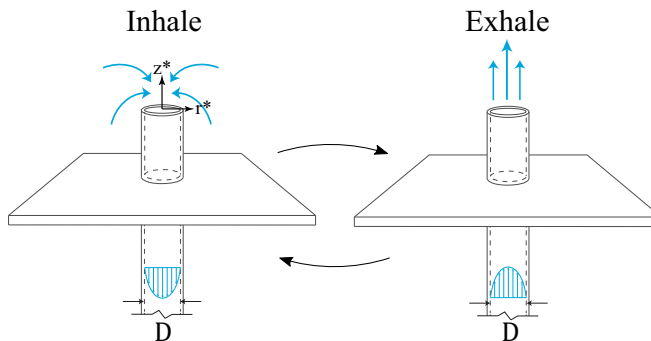
FIG. 1. Schematic of an idealized respiratory-type flow showing the inhale (left) and exhale (right) portions of the periodic flow cycle. Flow is inhaled and exhaled through a round tube that protrudes through a solid wall.

time-varying component at the orifice increases the number of governing parameters, and produces a wider range of relevant flow structures. We use a combination of experimental and numerical approaches to demonstrate the complex and nonlinear flow physics unique to respiratory-type flows. Time-resolved model results allow quantification of the dynamic exchange occurring with each cycle. We show that more inertial flows (i.e., higher Re) result in greater asymmetry between the inhale and exhale, which increases the efficiency of exchange with the external fluid environment. Focusing on the intermediate Re regime in which both viscosity and inertia are relevant to flow dynamics produces the most generalizable insights into fluid exchange processes across a broad range of respiratory-type flows of interest. The implications of these findings are discussed particularly in the context of olfaction.

II. METHODOLOGY

A. Model system and scaling parameters

We modeled an idealized respiratory-type flow consisting of an incompressible fluid that is periodically inhaled and exhaled through the orifice of a long, round tube located within a semi-infinite reservoir of initially quiescent fluid (Fig. 1). The laminar flow is driven by a cyclic flow rate $Q(t)$ within the tube; the cross-sectional average velocity is then $U(t) = 4Q/\pi D^2$, where D is the tube diameter. The mass flux across the orifice during one period T is prescribed to be zero: $\int_0^T U(t)dt = 0$. We define a characteristic tube velocity as the phase-averaged velocity magnitude u_ϕ, whose definition is provided below:

$$u_\phi = \frac{1}{T} \int_0^T |U(t)|dt. \tag{1}$$

It follows that for a given u_ϕ and T, the tidal volume V_0 is determined as follows:

$$V_0 = \frac{\pi D^2}{4} u_\phi \frac{T}{2}. \tag{2}$$

Using the characteristic velocity and diameter of the tube/orifice as a characteristic length scale, the phase-averaged Reynolds number is defined as

$$\text{Re}_\phi = \frac{u_\phi D}{\nu}, \tag{3}$$

where ν is the kinematic viscosity.

The Reynolds number can be expressed as a ratio of two timescales: the viscous timescale $t_{\text{viscous}} = D^2/\nu$, relative to the inertial timescale $t_{\text{inertial}} = D/u_\phi$. The periodic nature of respiratory-type flows introduces a third timescale, the respiration period T, which can be combined with t_{inertial} and t_{viscous} to define two more nondimensional parameters: the Strouhal number (Sr) and Womersley number (α^2). The definitions of Sr and α^2 are given by Eqs. (4) and (5), respectively:

$$\text{Sr} = \frac{t_{\text{inertial}}}{T} = \frac{D}{u_\phi T}, \tag{4}$$

$$\alpha^2 = \frac{t_{\text{viscous}}}{T} = \frac{2\pi D^2}{\nu T}. \tag{5}$$

In keeping with convention, α^2 is written with the period of oscillations as an angular frequency. A smaller Sr indicates that the transients in the flow are dominated by the inertial effects, while a smaller α^2 indicates that the transients in the flow are dominated by the viscous effects. Re_ϕ, Sr, and α^2 each provide a means for delineating between flow regimes. Note that these parameters are not mutually independent since $\alpha^2 = 2\pi \, \text{Sr} \, \text{Re}_\phi$.

If the inhale time (t_i) and exhale time (t_e) are not equal, then an additional timescale is introduced. We parametrize this factor as the ratio I:E $= t_i/t_e$. A large I:E ratio consists of a long, slow inhale followed by a short, intense exhale, whereas a small I:E ratio consists of a short, intense inhale followed by a long, slow exhale.

B. Governing equations and numerical methods

The model system is governed by the incompressible Navier-Stokes equation

$$\frac{\partial \mathbf{u}^*}{\partial t^*} + \mathbf{u}^* \cdot \boldsymbol{\nabla}^* \mathbf{u}^* = -\boldsymbol{\nabla}^* p^* + \text{Re}_\phi^{-1} \nabla^{*2} \mathbf{u}^* + \mathbf{g}^*, \tag{6}$$

and continuity equation

$$\boldsymbol{\nabla}^* \cdot \mathbf{u}^* = 0, \tag{7}$$

where vector quantities are denoted with bold font, and nondimensional quantities with an asterisk. Length, velocity, time, pressure, and body accelerations have been nondimensionalized by D, u_ϕ, D/u_ϕ, ρu_ϕ^2, and $D\mathbf{g}/u_\phi$, respectively. In the model, flow passes through a round tube with wall thickness $0.1D$ extending into a fluid domain with a radius of $60D$ and a total height of $120D$. The orifice of the tube is located $40D$ above the lower domain boundary. The center of the orifice defines the origin of the coordinate system with radial distance r and vertical distance z from the origin.

The model was initialized throughout with zero velocity and pressure, and approaches quasi-steady state after a sufficient number of cycles ($10T$). We are interested in the flow field around the orifice without the influence of nearby boundaries. We prescribed open boundaries for the domain sides and top, which were at least 60 diameters away from the region of interest. These boundary conditions were prescribed in the model as a pressure condition with a zero normal stress. The tube walls and tank bottom had impermeable, no-slip conditions ($\mathbf{u}^* = 0$). For the tube inlet and outlet, we specified a time-varying parabolic velocity profile 60 tube diameters below the tube orifice, with average flow velocity $U(t)$. For oscillating pipe flow, the in-tube flow profile deviates from the archetypal parabolic Poiseuille flow, and depends on the magnitude (Re_ϕ) and frequency (α^2) of periodic flow [34]. We maintained a consistent location of the lower boundary condition across all flow cases with changing Re_ϕ and α^2. While this impacted the in-tube velocity profile development, our current work focuses on the impact of Re_ϕ and α^2 on the flow field external to the tube.

Numerical simulations of the model system were performed via finite-element discretization of the governing equations [Eqs. (6) and (7)], using the COMSOL MULTIPHYSICS package. Model axisymmetry permitted using only two space variables (r, z) in cylindrical polar coordinates. The mesh was generated with local refinement around solid surfaces using triangular and quadrilateral elements. The z-component velocity served as an error indicator for the adaptive mesh scheme which

automatically increased the number of mesh elements by 70% each time the error criteria were not met. The mesh refinement was accomplished by bisecting the longest edge of mesh elements where the local error was largest [35]. The adaptive algorithm automatically generated multiple meshes in the course of a single simulation with greatest mesh density near the tube and in regions with larger velocity gradients. This iterative process of mesh refinement and local error estimation occurred at each time step. Second-order shape functions were used for both the fluid velocity and the pressure during discretization across the mesh elements [36]. We systematically increased the starting mesh size to confirm for model convergence and resolution.

The numerical integration scheme implemented a second-order implicit backward differentiation formula (BDF) with variable time steps adaptively chosen to meet relative and absolute tolerance criteria imposed on the truncation error [37,38]. Across multiple model test runs, we systematically decreased the tolerance criteria until the solutions converged. From this convergence study we conservatively chose 0.005 for the relative tolerance criteria. Given the highly transient, yet periodic, nature of the flow, we further constrained the time-stepping algorithm to a maximum time step of $0.0005T$. Additionally, integration schemes included terms for streamline and crosswind diffusion to account for numerical diffusion and to enhance stability. The nonlinear systems of equations were solved with a direct PARDISO solver [39,40].

Computed time-resolved flow fields were used to investigate convective exchange of fluid during a complete inhale and exhale cycle for different flow cases. We utilized Lagrangian particle tracking with an improved Euler forward numerical integration to map the spatial evolution of the fluid envelope inhaled or exhaled during a given cycle. For the exhalation envelope, we tracked the evolution of virtual particles initially placed across the tube orifice ($z^* = 0$, $0 \leqslant r^* \leqslant \frac{1}{2}$) at the beginning of the exhale. For the inhalation envelope, we repeated the process with the particles placed across the orifice at the end of the inhale and then integrated backward in time. Higher particle densities were required near the tube walls where velocity gradients and strain rates were highest. We define the reinhalation ratio r_I as

$$r_I = \frac{V_r}{V_0}, \tag{8}$$

where V_r is the volume of fluid reinhaled between the inhale and exhale.

We investigated 37 flow cases (Table I). These considered variations in Re_ϕ, overall period (T), forcing function, and I:E ratio. For a given forcing function and I:E, we ran simulations with three different Reynolds numbers ($Re_\phi = 1$, 10, and 100) and three different periods ($T = 1$, 5, and 10 s) for a total of nine combinations. We used two functions for $U(t)$ at I:E $= 1$: a sine wave, and a smooth function similar to a square wave shown in Fig. 2. The modified square wave incorporated error functions to control the rate at which the velocity transitioned between inhale and exhale as shown below:

$$U^*(t^*) = \begin{cases} \frac{1}{2}[\text{erf}(\frac{4}{\tau}t^* - 2) + 1], & 0 < t^* \leqslant \frac{1}{2} - \tau \\ \frac{1}{2}\{-\text{erf}[\frac{4}{\tau}(t^* - \frac{1}{2}) + 2] + 1\}, & \frac{1}{2} - \tau < t^* \leqslant \frac{1}{2} \\ \frac{1}{2}\{-\text{erf}[\frac{4}{\tau}(t^* - \frac{1}{2}) - 2] - 1\}, & \frac{1}{2} < t^* \leqslant \tau + \frac{1}{2} \\ \frac{1}{2}\{\text{erf}[\frac{4}{\tau}(t^* - \frac{1}{2}) - 6] - 1\}, & \tau + \frac{1}{2} < t^* \leqslant 1 \end{cases} \tag{9}$$

where U^* is nondimensionalized by u_ϕ, t^* is nondimensionalized by the period T, and the parameter τ controls the time to reach the maximum velocity. All flow cases used $\tau = 0.01$. As written, Eq. (9) applies for I:E$=1$, but can be adjusted for additional I:E cases as shown in Fig. 2. The function was chosen so that it was smooth for model convergence and consistent with experimental conditions described subsequently. We also completed nine simulations for I:E $= \frac{1}{2}$ and I:E $= 2$ using the same combinations of Re_ϕ and T that were used for the I:E $= 1$ case. Across the test cases, α^2 varied in the range between 7.3–73 and Sr varied between 0.012–12. In all cases, the kinematic viscosity was held constant at $\nu = 1 \times 10^{-6}$ m^2/s.

TABLE I. List of computed flow cases, grouped by the forcing functions shown in Fig. 2; cases 1–9 correspond to using Fig. 2(a), cases 10–19 correspond to Fig. 2(b), cases 20–28 correspond to Fig. 2(d), and cases 29–37 correspond to Fig. 2(c). In all cases, the kinematic viscosity used was $\nu = 1 \times 10^{-6}$ m²/s. The resulting inhalation ratios (r_I) are given in the final column.

Forcing function	I:E	Case No.	T (s)	u_ϕ (m/s)	V_0 (m³)	Re_ϕ	α^2	Sr	r_I
Sine	1	1	1	3.4×10^{-4}	3.1×10^{-9}	1	73	12	0.99
		2	1	3.4×10^{-3}	3.1×10^{-8}	10	73	1.2	0.87
		3	1	3.4×10^{-2}	3.1×10^{-7}	100	73	0.12	0.06
		4	5	3.4×10^{-4}	1.5×10^{-8}	1	15	2.3	0.98
		5	5	3.4×10^{-3}	1.5×10^{-7}	10	15	0.23	0.58
		6	5	3.4×10^{-2}	1.5×10^{-6}	100	15	0.023	0.02
		7	10	3.4×10^{-4}	3.1×10^{-8}	1	7.3	1.2	0.97
		8	10	3.4×10^{-3}	3.1×10^{-7}	10	7.3	0.12	0.41
		9	10	3.4×10^{-2}	3.1×10^{-6}	100	7.3	0.012	0.02
Mod. Sqw.	1	10	1	3.4×10^{-4}	3.1×10^{-9}	1	73	12	0.99
		11	1	3.4×10^{-3}	3.1×10^{-8}	10	73	1.2	0.83
		12	1	3.4×10^{-2}	3.1×10^{-7}	100	73	0.12	0.06
		13	5	3.4×10^{-4}	1.5×10^{-8}	1	15	2.3	0.97
		14	5	3.4×10^{-3}	1.5×10^{-7}	10	15	0.23	0.47
		15	5	3.4×10^{-2}	1.5×10^{-6}	100	15	0.023	0.01
		16	10	3.4×10^{-4}	3.1×10^{-8}	1	7.3	1.2	0.95
		17	10	3.4×10^{-3}	3.1×10^{-7}	10	7.3	0.12	0.27
		18	10	3.4×10^{-2}	3.1×10^{-6}	100	7.3	0.012	0.002
		19	100	3.4×10^{-2}	3.1×10^{-7}	1	0.73	0.12	0.87
Mod. Sqw.	0.5	20	1	3.4×10^{-4}	3.1×10^{-9}	1	73	12	0.99
		21	1	3.4×10^{-3}	3.1×10^{-8}	10	73	1.2	0.84
		22	1	3.4×10^{-2}	3.1×10^{-7}	100	73	0.12	0.10
		23	5	3.4×10^{-4}	1.5×10^{-8}	1	15	2.3	0.97
		24	5	3.4×10^{-3}	1.5×10^{-7}	10	15	0.23	0.55
		25	5	3.4×10^{-2}	1.5×10^{-6}	100	15	0.023	0.02
		26	10	3.4×10^{-4}	3.1×10^{-8}	1	7.3	1.2	0.95
		27	10	3.4×10^{-3}	3.1×10^{-7}	10	7.3	0.12	0.39
		28	10	3.4×10^{-2}	3.1×10^{-6}	100	7.3	0.012	0.01
Mod. Sqw.	2	29	1	3.4×10^{-4}	3.1×10^{-9}	1	73	12	0.99
		30	1	3.4×10^{-3}	3.1×10^{-8}	10	73	1.2	0.80
		31	1	3.4×10^{-2}	3.1×10^{-7}	100	73	0.12	0.04
		32	5	3.4×10^{-4}	1.5×10^{-8}	1	15	2.3	0.97
		33	5	3.4×10^{-3}	1.5×10^{-7}	10	15	0.23	0.30
		34	5	3.4×10^{-2}	1.5×10^{-6}	100	15	0.023	0.004
		35	10	3.4×10^{-4}	3.1×10^{-8}	1	7.3	1.2	0.95
		36	10	3.4×10^{-3}	3.1×10^{-7}	10	7.3	0.12	0.13
		37	10	3.4×10^{-2}	3.1×10^{-6}	100	7.3	0.012	0.002

III. EXPERIMENTAL COMPARISON

We performed laboratory experiments (Fig. 3) of an idealized respiratory-type flow for two cases ($\mathrm{Re}_\phi = 10$ and $\mathrm{Re}_\phi = 100$) to validate the flow features and dynamics observed in the numerical simulations. A cylindrical borosilicate glass tube with an inner diameter of 3.12 mm (outer diameter 4.96 mm) entered a 0.58 m × 0.58 m × 0.58 m acrylic tank and extended a vertical distance of 40 diameters above the tank bottom. To minimize apparatus boundary effects, the tank walls and the
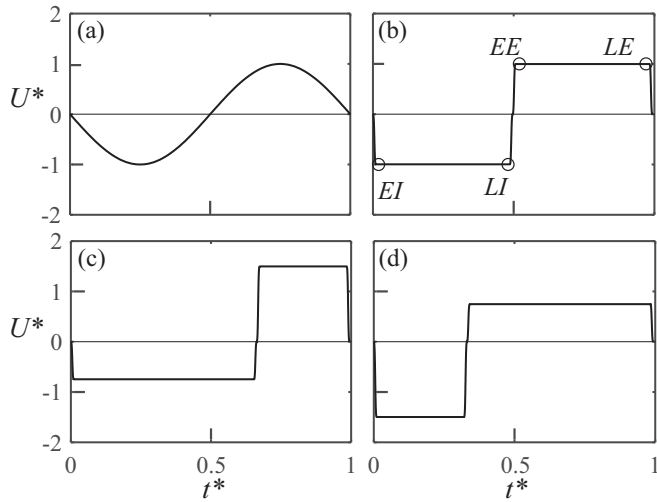
FIG. 2. Time-varying cross-sectional average nondimensional velocities used as forcing functions for the numerical simulations. For I:E=1, two forcing functions were used: a sine wave (a) and a modified square wave (b). The circles in (b) indicate the phase points referred to in Figs. 7–9, where EI, LI, EE, and LE correspond to "early inhale," "late inhale," "early exhale," and "late exhale." A modified square wave was also used with I:E = 2 (c) and I:E = 0.5 (d).
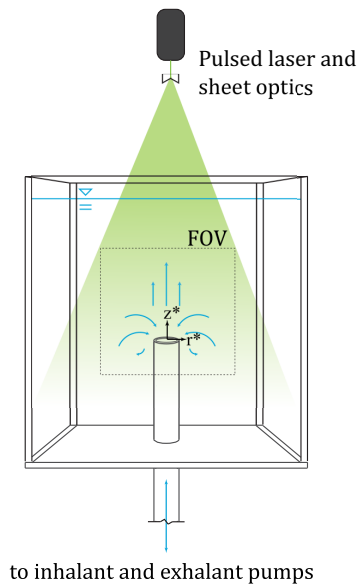

FIG. 3. Schematic showing the experimental apparatus. An Nd:YAG pulsed laser created a light sheet orientated to bisect the tube from above. A sCMOS camera (not shown) was oriented perpendicular to the laser sheet with a field of view (FOV) indicated by the dashed lines. A Y junction 60 diameters from the tube orifice connected the flow to two separate digital gear pumps controlling the flowrate through the tube, one dedicated to the inhale and one dedicated to the exhale.
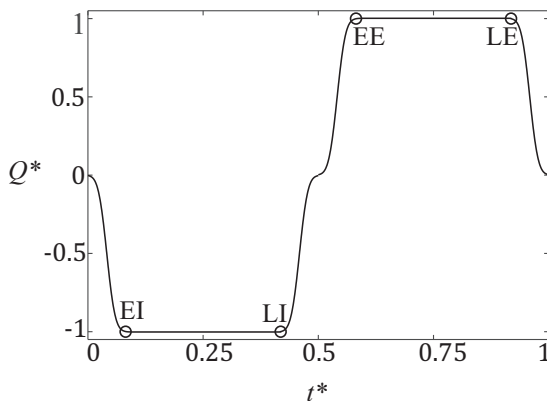
FIG. 4. Pump flow rate signal used to drive inhale and exhale pumps in the experiments. The circles mark phase points at which image pairs were collected for analysis by particle image velocimetry (PIV). The labels on the phase points correspond to Figs. 5 and 6, where EI, LI, EE, and LE correspond to "early inhale," "late inhale," "early exhale," and "late exhale."

free surface were located 85 diameters away from the tube center [14]. For the $Re_\phi = 10$ case, we used mineral oil as the working fluid, and for the $Re_\phi = 100$ case, we used water. A system of computer-controlled gear pumps and valves were used to periodically drive flow in and out of the tube orifice. The flow rate was programed as a series of error functions to better account for the pump inertial response times, producing the forcing function shown in Fig. 4.

We quantified the resulting respiratory-type flows interior and exterior to the orifice using particle image velocimetry (PIV). We seeded the tank and tube fluid with neutrally buoyant particles (20 μm, 1.03 g/cc, polyamide microspheres, Dantec Dynamics PSP-20). For the chosen diameter and flow velocities, particles closely adhere to fluid streamlines (low Stokes number). An adjustable lens doublet focused and expanded a double-pulsed Nd:YAG laser (532 nm) into a 500-μm-thick sheet in the r-z plane that passed through the tube center. We imaged particles in the light sheet in a field of view centered around the tube orifice with an sCMOS camera (monochrome, 16 bit, 2160 × 2560). We used PIV best practices to optimize correlation strength and signal-to-noise ratio including seeding densities resulting in 8–10 particles per interrogation subwindow, particle image diameters near 3 px, and pulse separation times between images pairs that yielded particle displacements of approximately one-quarter the width of an interrogation window [41]. The resultant PIV image sets were analyzed using DAVIS software (8.2.3, Lavision GmbH) and best correlation practices were used to maximize the dynamic range and spatial resolution of the velocity measurement, including multipass cross correlation with overlapping (50%–75%) windows of decreasing sizes (typically 64 px–32 px) shaped to local flow gradients. After initiating the pumps, we waited for the system to reach quasi-steady state before we collected 4 image pairs per cycle for 1000 cycles. For comparison with numerical simulations, we computed ensemble average velocities of all 1000 velocity field realizations at each of the 4 phase points (represented by "o" symbols in Fig. 4) at which PIV image pairs were obtained.

We performed numerical simulations that were parameter matched in geometry, forcing, and nondimensional flow parameters to the experimental measurements. Figures 5 ($Re_\phi = 10$) and 6 ($Re_\phi = 100$) show comparisons of the numerical (top row) and experimental (bottom row) velocity magnitude field (grayscale) at each of the four phase points (columns). The figures show excellent correspondence of both structural flow features and velocity magnitudes between the simulations and experiments. In the experimental velocity data, optical occlusion from the orifice in the raw images led to correlation degradation in the PIV analysis; the tube drawn onto the figures masks
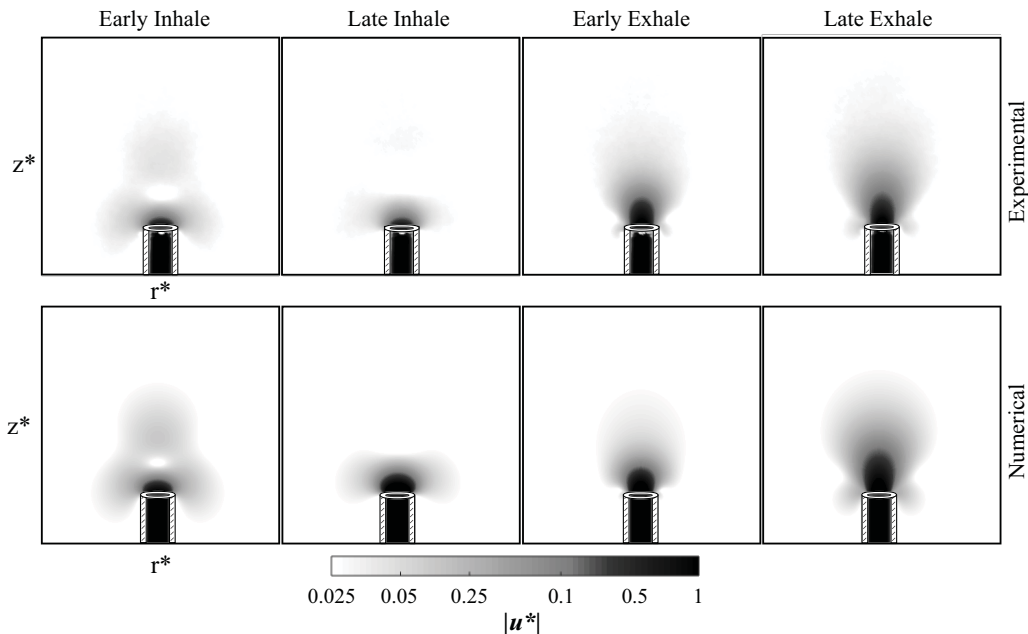
FIG. 5. Velocity magnitude plots comparing the experimental observations (top row) to the numerical results (bottom row). All figures are for $Re_\phi = 10$, with a consistent forcing function between experiments and simulations. Each column corresponds to one of the four phase points indicated in Fig. 4.

regions of nonphysical data. Other minor variations in flow structure and/or velocity magnitude are likely due to inertial response of the pump and other experimental artifacts.

IV. RESULTS

A. Flow fields

To illustrate the quasi-steady-state flow dynamics over the course of an inhale and exhale cycle, we present numerically obtained flow fields at four phase points for a representative flow case at $Re_\phi = 1$ (Fig. 7). The chosen flow case (Table I, case No. 13) is forced with the modified square wave, and the four listed phase points (early inhale, late inhale, early exhale, late exhale) correspond to the locations indicated by the circles in Fig. 2(b). The I:E ratio is 1, Sr = 2.3, and $\alpha^2 = 15$. Each panel in Fig. 7 shows the instantaneous velocity field in an r-z plane passing through the orifice center. Arrows indicate local flow direction; they are shaded with a logarithmic grayscale to indicate velocity magnitude. Velocity magnitudes attenuate rapidly with distance from the inlet orifice and decay to less than $|\mathbf{u}^*| = 0.01$ within a few orifice diameters. Each panel shows instantaneous velocity contours for $|\mathbf{u}^*| = 0.05$ (solid lines) and $|\mathbf{u}^*| = 0.01$ (dashed lines), indicating where velocities have decayed to 5% and 1% of u_ϕ, respectively. Representative streamlines are shown with solid gray lines.

If the inhalant phase [Figs. 7(a) and 7(b)] were instead an ideal steady-state point sink, flow would be spherically symmetric with pure radial inflow and circular velocity contours in the r-z plane. Likewise, if the exhalant phase [Figs. 7(c) and 7(d)] were an ideal steady-state point source, flow would be spherically symmetric with pure radial outflow and circular velocity contours. In each case, these idealized flow magnitudes would decay as r^{-2} from the origin. The unsteady respiratory-type flow in Fig. 7 deviates from these idealized sink and source flows for several reasons. First, the orifice is finite in size, and has a directional orientation. Second, the solid walls of the tube
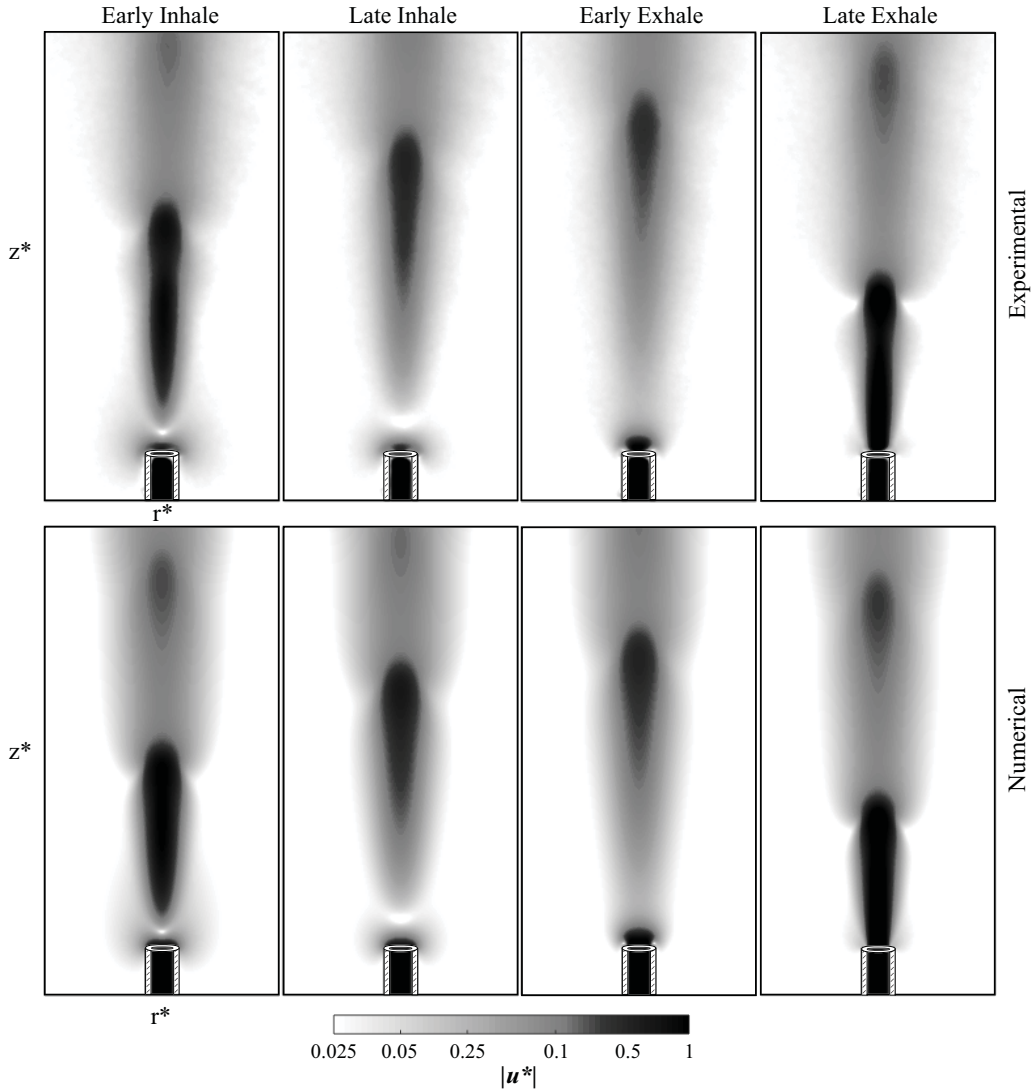
FIG. 6. Velocity magnitude plots comparing experimental (top row) and numerical (bottom row) results for $Re_\phi = 100$.

impose impermeable and no-slip boundary conditions that result in the production of unsteady boundary layers on the tube interior and exterior. Third, inertial effects produce spatially varying lags in flow response to unsteady forcing. Within the tube, the second and third effects combine to produce a time-varying velocity profile typical of pulsatile pipe flow [34] that also develops spatially downstream of the orifice during inhalation over a characteristic flow development length [42]. Outside of the tube, the three effects combine to produce the complex spatiotemporal flow structure evident in Fig. 7.

At the start of the inhalant phase [Fig. 7(a)], development of inward flow along the z axis is retarded due to residual outward momentum from the previous exhalant phase [Fig. 7(d)]; the residual exhale momentum is preferentially aligned along the z axis due to inertial effects, and is evidenced by the dimple at the top of the 1% (dashed) velocity contour in Fig. 7(a). By the end of the inhale [Fig. 7(b)], viscous diffusion of inward momentum has largely negated the residual outward
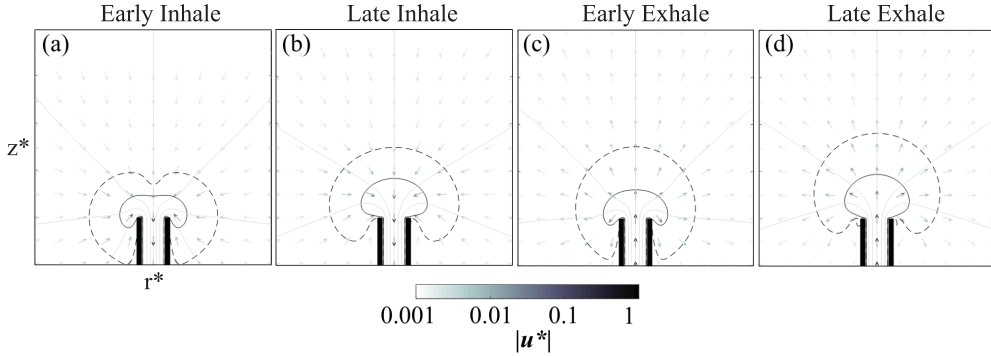
FIG. 7. Instantaneous velocity fields in the r-z plane centered at the orifice for $\mathrm{Re}_\phi = 1$ numerical simulations (Table I, case No. 13: $\alpha^2 = 15$ and Sr = 2.3). Velocity fields are shown for each of the four phase points indicated in Fig. 2(b). Arrows indicate velocity direction and are color coded to indicate velocity magnitude. Streamlines are shown as gray lines. Contours of constant velocity magnitude for $|\mathbf{u}^*| = 0.01$ and 0.05 are plotted as dashed and solid black lines, respectively. The tube walls are indicated as black rectangles.

momentum and the axial dimple in the 1% velocity contour has disappeared. Boundary-layer development on the outside of the tube is evidenced in Figs. 7(a) and 7(b) by the separation of the 1% velocity contour from the outside tube wall. At the exhale onset [Fig. 7(c)], the velocity profile within the tube is relatively flat (as the interior boundary layers are still forming); this results in a relatively uniform vertical pulse of fluid evidenced by the flat 5% (solid) velocity contour near the z axis. By the end of the exhale [Fig. 7(d)], the velocity profile within the tube approaches a parabolic distribution, and the 5% contour becomes more circular.

We now consider the effect of Re_ϕ on the inhale and exhale flow dynamics. We increase Re_ϕ while holding α^2 constant (this results in a decrease in Sr). This is consistent with increasing u_ϕ while holding other parameters (D, ν, and T) constant. Numerically obtained flow fields for $\mathrm{Re}_\phi = 10$ (Sr = 0.23, Table I, case No. 14) and $\mathrm{Re}_\phi = 100$ (Sr = 0.023, Table I, case No. 15) are presented in Figs. 8 and 9, respectively.

More pronounced deviations from the ideal point sink and source flow manifest in the $\mathrm{Re}_\phi = 10$ case (Fig. 8). During the inhale [Figs. 8(a) and 8(b)], the 2D velocity contours now form a three-lobed structure where fluid flows outward in the axial lobe and inward in the off-axis lobes.
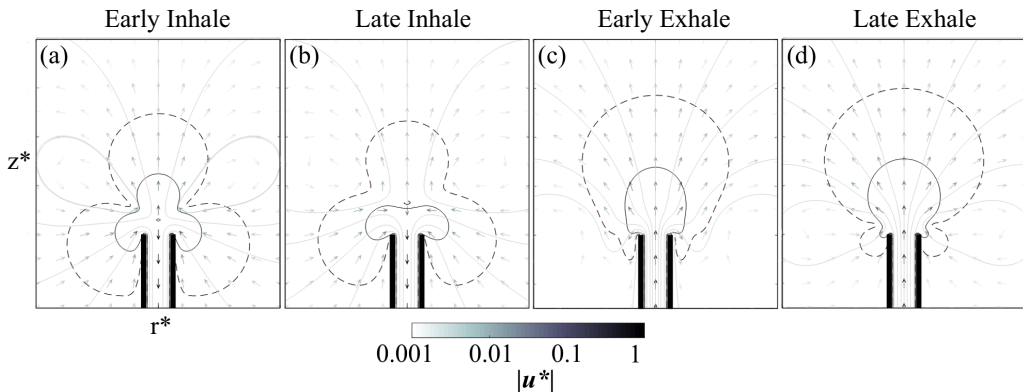

FIG. 8. Instantaneous velocity field for $\mathrm{Re}_\phi = 10$ numerical simulations (Table I, case No. 14: $\alpha^2 = 15$ and Sr = 0.23). Velocity direction, magnitude, and streamlines are shown in the same manner as Fig. 7.
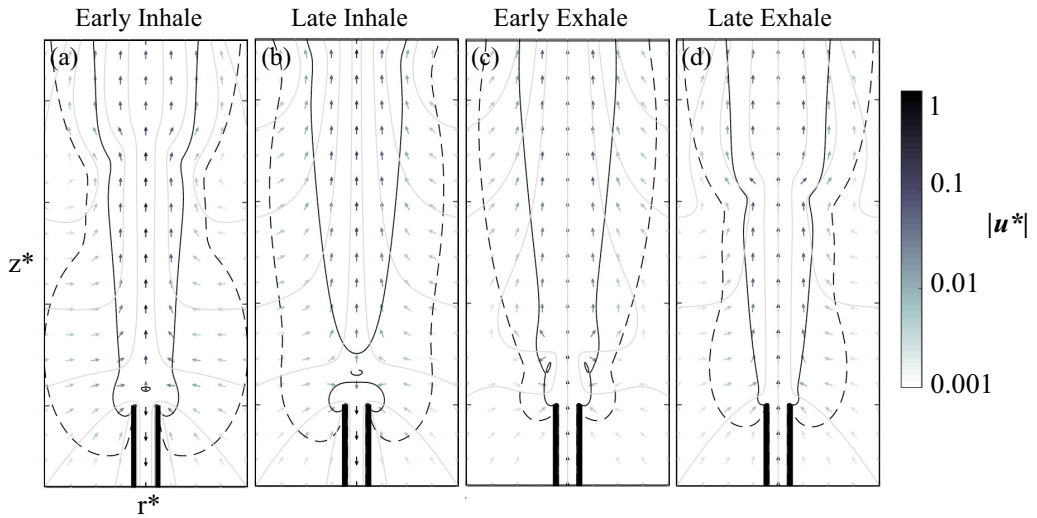
FIG. 9. Instantaneous velocity field for $Re_\phi = 100$ numerical simulations (Table I, case No. 15: $\alpha^2 = 15$ and Sr = 0.023). Velocity direction, magnitude, and streamlines are shown in the same manner as Fig. 7.

The outward axial flow results from residual inertia persisting from the previous exhale. In the off-axis lobes, the inertial effect of the previous exhale is weaker and inward flow has already initiated. By the end of the inhale [Fig. 8(b)], viscous effects retard the residual outward flow such that the axial lobe in the 5% $|\mathbf{u}^*|$ velocity contour (solid) disappears. During the exhale [Figs. 8(c) and 8(d)], inertial effects associated with the higher Re_ϕ results in weak jetlike behavior, with velocity contours that are elongated in the axial direction. By the end of the exhale [Fig. 8(d)], viscous entrainment has induced off-axis recirculation, with upward flow along the tube exterior. This recirculation reinforces subsequent formation of the off-axis lobes seen in the early inhale [Fig. 8(a)].

For $Re_\phi = 100$ (Fig. 9), the system transitions to a more inertial regime dominated by a persistent jetlike structure throughout the inhale and exhale cycle. Directly outside the orifice, flow reversal at the onset of the inhale [Fig. 9(a)] results in a saddle point in the velocity field, associated with a local minimum in the velocity magnitude. Beyond the saddle point, significant outward flow ($|\mathbf{u}^*| >$ **5**%) persists throughout the inhale and exhale cycle. The pronounced jet structure exhibits starting jet behavior with vortex formation. The annular vortex appears in the early exhale velocity field [Fig. 9(c)] as a pair of small elliptical 5% velocity contours, and later [Fig. 9(d)] as a narrowing of the 5% contour as the velocity decays. The jet structure continuously entrains off-axis fluid; radial entrainment merges with outward advection during the exhale and enhances the lateral biasing of flow during the subsequent inhale.

B. Exchange ratio

We use a Lagrangian analysis with the computed flow fields to map spatial distributions of the volumes of fluid that are inhaled and subsequently exhaled through the orifice. In particular, we compute the overlap region between these volumes, which corresponds to the portion of the exhaled volume that is reinhaled on the following inhale phase (i.e., V_r). Figure 10 shows the process used to obtain bounding envelopes of inhalation and exhalation volumes at different times for the same representative flow case (Table I, case No. 13) at $Re_\phi = 1$ shown in Fig. 7. The dark red (dashed) line in Fig. 10(a) shows a two-dimensional slice of the envelope bounding the total inhalation volume at the beginning of the inhale. Lighter shades of red (dashed lines) indicate the location of the envelope at later times as the volume is drawn into the orifice. Figure 10(b) shows the time progression of the
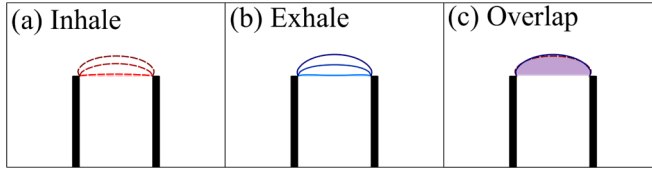
FIG. 10. Progression of the inhale and exhale bounding envelopes resulting from the velocity field shown in Fig. 7 ($Re_\phi = 1$, Table I case No. 13). In the left panel (a), the darkest red (dashed) line indicates the spatial extent of the total inhaled volume, with lighter shades of red (dashed lines) indicating later times during the inhale. The middle panel (b) shows the extent of the total exhaled volume, with darker shades of blue (solid lines) indicating later times. The right panel (c) compares the initial extent of the inhaled volume (red dashed line) to the final extent of the exhaled volume (blue solid line). The overlapping region corresponding to the reinhaled volume is shaded.

exhalation volume. The lighter shades in this panel indicate earlier times with the darkest shade of blue (solid line) marking the location of the envelope at the end of the exhale. The boundaries of the total inhalation and exhalation volumes from the first two panels of the figure are reproduced in Fig. 10(c); for this Re_ϕ, the two boundaries are so similar that they are hard to distinguish from one another. The shaded region indicates the volume that gets reinhaled and reexpelled with each cycle. The highly viscous nature of this low-Re_ϕ flow case causes the flow to be nearly reversible. This results in a high degree of symmetry between the distributions of the inhale and exhale volumes, with a corresponding reinhalation ratio $r_I = 0.97$ (where an exchange ratio of unity would constitute complete reinhalation).

Figures 11 and 12 similarly show the time progression of the bounding inhalation and exhalation envelopes for $Re_\phi = 10$ and 100 cases, respectively (Table I, cases No. 14 and No. 15). Increasing Re_ϕ drives an increasing asymmetry between the inhale and exhale flow fields, evidenced as more axial, inertially driven flow outward and more laterally biased, viscous flow inward (Figs. 8 and 9). This increased flow asymmetry alters the progression of the bounding envelopes as well as their final extent seen in Figs. 11(c) and 12(c). The reduction in reinhaled fluid (shaded region) relative to the tidal volume translates to an r_I of only 0.47 for the $Re_\phi = 10$ case. Hardly any reinhalation occurs during the $Re_\phi = 100$ case, with $r_I = 0.01$.

For the inhale and exhale volume comparisons shown in Figs. 10–12, Re_ϕ was increased while holding α^2 constant. This caused a reduction in Sr and an increase in the tidal volume V_0 (the latter is evidenced by the increased size of the volume envelopes). Figure 13 shows final bounding envelopes and overlap regions for $Re_\phi = 1$, 10, and 100, all for Sr = 0.12, and fixed V_0 (Table I, cases No.
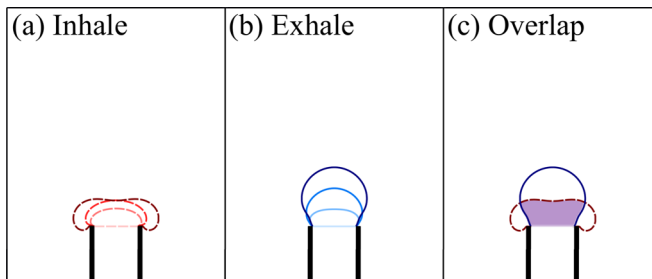

FIG. 11. $Re_\phi = 10$ bounding envelopes over the course of an inhale and exhale cycle resulting from the velocity field shown in Fig. 8 (Table I, case No. 14). As in Fig. 10, the time evolution of the bounding envelopes is shown separately for the inhale (a) and exhale (b); a comparison is shown in the right panel (c) to illustrate the overlapping region corresponding to the reinhaled volume.
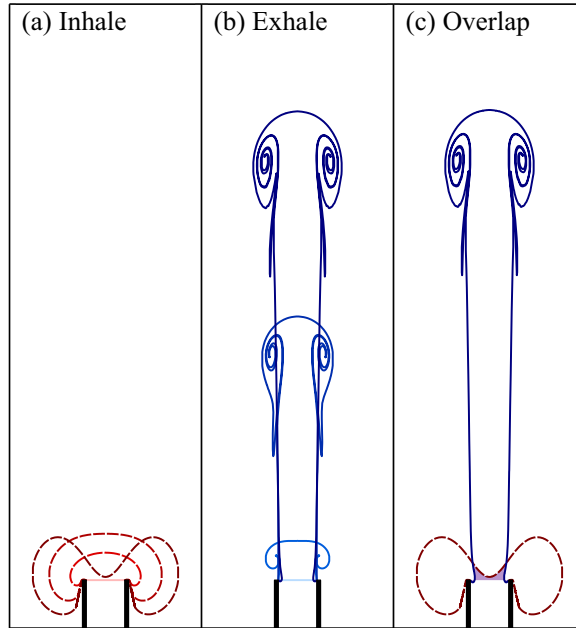
FIG. 12. $Re_\phi = 100$ bounding envelopes over the course of an inhale and exhale cycle resulting from the velocity field shown in Fig. 9 (Table I, case No. 15). The progression of the bounding envelopes is shown as in Fig. 10. To accommodate the larger tidal volume, the figure spans a larger range of r^* and z^* for this case.

19, No. 17, and No. 12). For increasing Re_ϕ, the inertial component of the flow increases and the symmetry between the inhale and exhale decreases. The shaded region indicative of the V_r also dramatically decreases with increasing Re_ϕ moving from the left panel to the right panel. Since the tidal volume is the same in all three cases, the decrease in V_r corresponds to an inverse relationship between r_I and Re_ϕ, where $r_I = 0.87$, 0.27, and 0.06 for $Re_\phi = 1$, 10, and 100, respectively.

The reinhalation ratio r_I has a strong dependence on Re_ϕ [Fig. 14(a)]. At lower Re_ϕ, r_I asymptotes to the upper limit of 1, corresponding to complete reinhalation. As Re_ϕ increases, r_I decreases dramatically. For a given Re_ϕ, r_I also decreases with α^2 (indicated by the open red, shaded blue, and filled black symbols). Increasing α^2 (e.g., by decreasing the period T) constrains
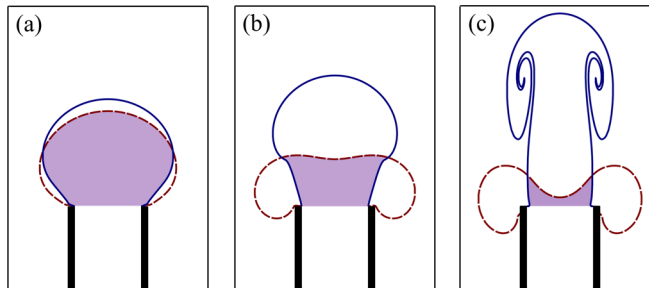

FIG. 13. Effect of Re_ϕ on the bounding envelopes over the course of an inhale and exhale cycle for a fixed tidal volume V_0. The respective bounding envelopes are shown for increasing Re_ϕ: (a) $Re_\phi = 1$, (b) $Re_\phi = 10$, and (c) $Re_\phi = 100$ (Table I, cases No. 19, No. 17, and No. 12, respectively). In all three panels, the bounding envelope of the total inhalant volume (red dashed) and exhalant volume (blue solid) are compared to indicate the reinhaled volume (shaded region).
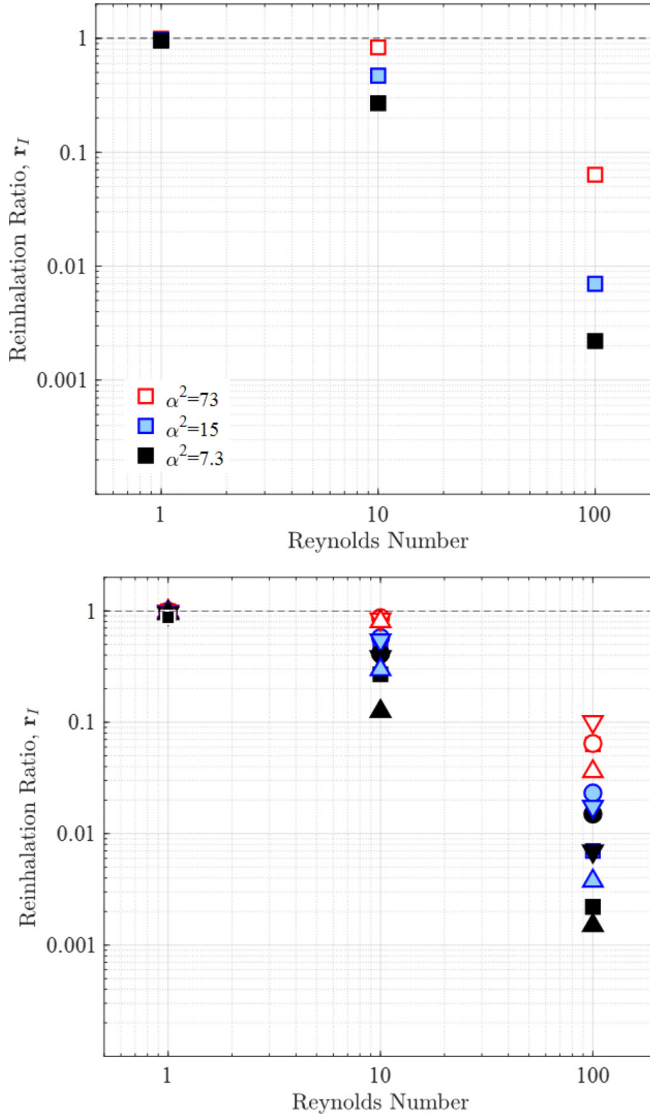
FIG. 14. Reinhalation ratio dependence on relevant flow parameters including Reynolds number Re_ϕ. Colors indicate different α^2 values. The top panel shows results for a single forcing function (cases Nos. 10–19: square wave with I:E=1). The bottom panel shows the results for all 37 cases listed in Table I with different symbols indicating different forcing functions and I:E ratios (sine wave: circles, square wave with I:E=1: squares, square wave with I:E= $\frac{1}{2}$: down-pointing triangles, I:E=2: up-pointing triangles).

the Reynolds-induced flow asymmetry from producing significantly different inhale and exhale volumes. To demonstrate that the effects of Re_ϕ and α^2 on r_I shown in Fig. 14(a) are not specific to the choice of forcing function or I:E ratio, we generalize the results by including all 37 flow cases in Fig. 14(b). The additional cases include sine waves (circles) and nonunity I:E square waves (triangles), all color coded by α^2 as in Fig. 14(a). At a given Re_ϕ, the reinhalation ratio does increase somewhat with decreasing I:E. At higher I:E, more time is spent inhaling, but the compensatory increase in the intensity of the exhale adds to the jetlike formation responsible for driving down r_I. Conversely for lower I:E, the longer, slower exhale is less inertial and maintains

more symmetry with the inhale phase. Sinusoidal forcing functions followed the same trends as the modified square wave forcing with respect to Re_ϕ and α^2. However, at $Re_\phi = 100$, an increase in reinhalation (compared to the corresponding I:E=1 square wave) is likely due to the more gradual change in velocity during transitions between inhale and exhale. The higher r_I indicates that the flow field maintains for more symmetry between phases. While other parameters exhibit meaningful trends (e.g., α^2 and I:E), Fig. 14(b) demonstrates that r_I most dramatically depends on Re_ϕ.

V. DISCUSSION

Our motivation to study respiratory-type flows stems from an interest in olfaction and respiration. Most animals do not passively sample their environment, but actively obtain odor samples and metabolites by sniffing and breathing. In considering the rich evolutionary variety of nose morphologies and behaviors associated with olfaction and respiration, we recognized a need to better understand the basic physical mechanisms involved that transcend complexities unique to particular species or individuals. We identified essential parameters (including Re and α^2) influencing the degree of asymmetry between the inhale and exhale fluid motions, thereby changing the efficiency of exchange during respiratory-type flows. These results suggest that adjustments to these parameters (e.g., through breathing rate or tidal volume) at evolutionary or behavioral timescales could provide a strategy for improving olfaction and respiration.

Previous studies have argued that flow dynamics associated with olfaction are partly responsible for the ability of many animals to detect chemical signals at astonishingly low concentrations which rival even the most sensitive analytic equipment [1]. Among these studies, some have considered not only the complicated flow patterns occurring internal to the nares, but also the external flow patterns. For example, the aerodynamic reach of the inhale allows for stereo sensing in both canine [43] and rat [10] nasal morphology. In canines, a directed jet during the exhale allows them to entrain fluid samples from further afield and liberate odors from surfaces for enhanced detection [1,43–45]. Interestingly, canine sniff rates tend to vary little between 4–7 Hz whereas tidal volume scales with body size [46]. Rats typically sniff at a rate of 15 Hz, but behavioral changes in sniffing rate occur in anticipation of odor information [47], in response to different odor stimuli or tasks [48,49], and to discriminate between background odorants and other odorants of interest [50]. These observed sampling behaviors suggest a physical mechanism for efficiently obtaining odorant information from the environment.

Human subjects also display highly variable breathing rates, flow patterns, and tidal volumes depending on the activity (e.g., sleeping, exercising, active sniffing, etc.), and across individuals [51,52]. Despite the wide range of tidal volumes and breathing rates, typical airflow patterns can be predicted by treating the system as an optimization problem to maximize oxygen uptake with minimal energy expenditure [53]. Using a cast of the human upper respiratory tract and flow visualization techniques, Haselton and Sperandio [11] also found that the highly efficient exchange of fluid during quiet respiration results in very little rebreathing of exhaled gas. With respect to olfaction, Sobel *et al.* [54]. showed that air flow rate and duration are key parameters for the detection threshold of odors with observed differences in sampling modes and even across the different nares of an individual.

Active changes and natural variation in sniffing and breathing suggest that animals may modulate the physical exchange of fluid with their surrounding environment. While our study demonstrates that animals could vary Re or α^2 in order to minimize reinhalation of previously sampled fluid, a range of other factors will add to the complexity of the problem in less idealized scenarios. For example, the results of this study already indicate that varying the I:E ratio at intermediate Re allows for differentially varying viscous and inertial effects in the inhale and exhale flow phases. The results of this study represent the advection-dominated case and provide a valuable reference point. However, it may be necessary to fully account for the scalar diffusivity of the exchanged substance in some specific cases. Additionally, future studies are needed to rigorously address the role of flow factors (e.g., I:E ratio), morphological factors (e.g., orifice proximity to a body and

dual nares), and ambient conditions (e.g., crossflows and turbulence). Continued efforts using a fundamental fluid mechanics approach can provide a more holistic understanding of the dynamics common to all respiratory-type flows.

VI. CONCLUSION

A numerical model of a geometrically idealized, respiratory-type flow was used to investigate the spatiotemporal flow dynamics exterior to the orifice as function of the phase-averaged Reynolds number (Re_ϕ), the Womersely number (α^2), and the Strouhal number (Sr). For the highly viscous low-Re_ϕ case, the flow exhibits a high degree of symmetry and reversibility between the inhale and exhale, and exhibits features reminiscent of an ideal point source and sink. At higher Re_ϕ, increased residual inertia during the exhale creates a jetlike flow structure with outward axial flow persisting throughout the entire inhale and exhale flow cycle. The spatiotemporal dynamics of the underlying flow structures strongly affect the reinhalation ratio, the amount of previously exhaled fluid that is subsequently reinhaled. The exchange ratio asymptotes to the upper limit ($r_I = 1$) at lower Re_ϕ, but decreases rapidly with increasing Re_ϕ. Additionally, the exchange ratio exhibits a weaker dependence on α^2 and I:E. As the period of forcing relative to the viscous and inertial timescales increases, r_I decreases. This work suggests that in the context of biologically relevant, respiratory-type flows such as olfaction and respiration, organisms can enhance the exchange of previously exhaled fluid with fresh fluid from the surrounding environment by modulating the asymmetries in the periodic flow structures.

[1] G. S. Settles, Sniffers: Fluid-dynamic sampling for olfactory trace detection in nature and homeland security- the 2004 freeman scholar lecture, J. Fluids Eng. **127**, 189 (2005).

[2] K. F. Liem, Form and function of lungs: The evolution of air breathing mechanisms, Am. Zool. **28**, 739 (1988).

[3] D. B. Chadwick and J. L. Largier, Tidal exchange at the bay-ocean boundary, J. Geophys. Res.: Oceans **104**, 29901 (1999).

[4] D. Parker, D. Norris, and A. Nelson, Tidal exchange at golden gate, J. Environ. Eng. Division **98**, 305 (1972).

[5] T. Awaji, Water mixing in a tidal current and the effect of turbulence on tidal exchange through a strait, J. Phys. Oceanogr. **12**, 501 (1982).

[6] E. E. Southwick and R. F. Moritz, Social control of air ventilation in colonies of honey bees, Apis mellifera, J. Insect Physiol. **33**, 623 (1987).

[7] R. F. Moritz and R. M. Crewe, Air ventilation in nests of two African stingless bees Trigona denoiti and Trigona gribodoi, Experientia **44**, 1024 (1988).

[8] J. O. Dabiri, S. P. Colin, J. H. Costello, and M. Gharib, Flow patterns generated by oblate medusan jellyfish: field measurements and laboratory analyses, J. Exp. Biol. **208**, 1257 (2005).

[9] M. J. McHenry, Comparative biomechanics: The jellyfish paradox resolved, Curr. Biol. **17**, R632 (2007).

[10] D. A. Wilson and R. M. Sullivan, Respiratory airflow pattern at the rat's snout and an hypothesis regarding its role in olfaction, Physiol. Behav. **66**, 41 (1999).

[11] F. Haselton and P. Sperandio, Convective exchange between the nose and the atmosphere, J. Appl. Physiol. **64**, 2575 (1988).

[12] P. K. Kundu, I. M. Cohen, and H. Hu, *Fluid Mechanics*, 3rd ed. (Academic, San Diego, 2004), p. 280.

[13] P. A. Jumars, Boundary-trapped, inhalant siphon and drain flows: Pipe entry revisited numerically, Limnol. Oceanogr.: Fluids Environ. **3**, 21 (2013).

[14] A. C. True and J. P. Crimaldi, Hydrodynamics of viscous inhalant flows, Phys. Rev. E **95**, 053107 (2017).

[15] N. Didden, On the formation of vortex rings: rolling-up and production of circulation, Z. Angew Math. Phys. **30**, 101 (1979).

[16] A. Glezer, The formation of vortex rings, Phys. Fluids **31**, 3532 (1988).

[17] C. Schram and M. L. Riethmuller, Vortex ring evolution in an impulsively started jet using digital particle image velocimetry and continous wavelet analysis, Meas. Sci. Technol. **12**, 1413 (2001).

[18] A. Glezer and M. Amitay, Synthetic jets, Annu. Rev. Fluid Mech. **34**, 503 (2002).

[19] B. L. Smith and A. Glezer, The formation and evolution of synthetic jets, Phys. Fluids **10**, 2281 (1998).

[20] B. L. Smith and G. W. Swift, A comparison between synthetic jets and continuous jets, Exp. Fluids **34**, 467 (2003).

[21] J. Béra, M. Michard, N. Grosjean, and G. Comte-Bellot, Flow analysis of two-dimensional pulsed jets by particle image velocimetry, Exp. Fluids **31**, 519 (2001).

[22] J. E. Cater and J. Soria, The evolution of round zero-net-mass-flux jets, J. Fluid Mech. **472**, 167 (2002).

[23] J. M. Shuster and D. R. Smith, Experimental study of the formation and scaling of a round synthetic jet, Phys. Fluids **19**, 045109 (2007).

[24] D. Greenblatt and I. Wygnanski, Dynamic stall control by periodic excitation, Part 1: NACA 0015 parametric study, J. Aircraft **38**, 430 (2001).

[25] M. Amitay and A. Glezer, Aerodynamic flow control using synthetic jet actuators, *Control of Fluid Flow* (Springer, Berlin, 2006), pp. 45–73.

[26] H. Choi, W.-P. Jeon, and J. Kim, Control of flow over a bluff body, Annu. Rev. Fluid Mech. **40**, 113 (2008).

[27] L. N. Cattafesta III and M. Sheplak, Actuators for active flow control, Annu. Rev. Fluid Mech. **43**, 247 (2011).

[28] S. G. Mallinson, J. Reizes, and G. Hong, An experimental and numerical study of synthetic jet flow, Aeronaut. J. **105**, 41 (2001).

[29] Z. Trávníček and V. Tesař, Annular synthetic jet used for impinging flow mass-transfer, Int. J. Heat Mass Transfer **46**, 3291 (2003).

[30] M. B. Gillespie, W. Z. Black, C. Rinehart, and A. Glezer, Local convective heat transfer from a constant heat flux flat plate cooled by synthetic air jets, J. Heat Transfer **128**, 990 (2006).

[31] M. Arik, Local heat transfer coefficients of a high-frequency synthetic jet during impingement cooling over flat surfaces, Heat Transfer Eng. **29**, 763 (2008).

[32] M. Chaudhari, B. Puranik, and A. Agrawal, Heat transfer characteristics of synthetic jet impingement cooling, Int. J. Heat Mass Transfer **53**, 1057 (2010).

[33] T. Persoons, A. McGuinn, and D. B. Murray, A general correlation for the stagnation point Nusselt number of an axisymmetric impinging synthetic jet, Int. J. Heat Mass Transfer **54**, 3900 (2011).

[34] S. Uchida, The pulsating viscous flow, superposed on the steady laminar motion of incompressible fluid in a circular pipe, J. Appl. Math. Phys. **7**, 403 (1956).

[35] R. Verfürth, A posteriori error estimation and adaptive mesh-refinement techniques, J. Comput. Appl. Math. **50**, 67 (1994).

[36] P. M. Gresho and R. L. Sani, *Incompressible Flow and the Finite Element Method, Advection-Diffusion* (Wiley, Chichester, 1998), Vol. 1.

[37] R. K. Brayton, F. G. Gustavson, and G. D. Hachtel, A new efficient algorithm for solving differential-algebraic systems using implicit backward differentiation formulas, Proc. IEEE **60**, 98 (1972).

[38] A. C. Hindmarsh, P. N. Brown, K. E. Grant, S. L. Lee, R. Serban, D. E. Shumaker, and C. S. Woodward, Sundials: Suite of nonlinear and differential/algebraic equation solvers, ACM Trans. Math. Software **31**, 363 (2005).

[39] O. Schenk, K. Gärtner, W. Fichtner, and A. Stricker, Pardiso: A high-performance serial and parallel sparse linear solver in semiconductor device simulation, Future Gen. Comput. Syst. **18**, 69 (2001).

[40] O. Schenk and K. Gärtner, Solving unsymmetric sparse systems of linear equations with pardiso, Future Gen. Comput. Syst. **20**, 475 (2004).

[41] M. Raffel, C. E. Willert, S. T. Wereley, and J. Kompenhans, *Particle Image Velocimetry; A Practical Guide*, 2nd ed. (Springer, Berlin, 2007).

[42] A. C. True and J. P. Crimaldi, High dynamic range particle image velocimetry analysis of viscous inhalant flows, Phys. Fluids **31**, 103605 (2019).

[43] B. A. Craven, E. G. Paterson, and G. S. Settles, The fluid dynamics of canine olfaction: unique nasal airflow patterns as an explanation of macrosmia, J. R. Soc., Interface **7**, 933 (2010).

[44] G. S. Settles, D. A. Kester, and L. J. Dodson-Dreibelbis, The external aerodynamics of canine olfaction, in *Sensors and Sensing in Biology and Engineering* (Springer, Berlin, 2003), pp. 323–335.

[45] M. E. Staymates, W. A. MacCrehan, J. L. Staymates, R. R. Kunz, T. Mendum, T.-H. Ong, G. Geurtsen, G. J. Gillen, and B. A. Craven, Biomimetic sniffing improves the detection performance of a 3D printed nose of a dog and a commercial trace vapor detector, Sci. Rep. **6**, 36876 (2016).

[46] W. R. Stahl, Scaling of respiratory variables in mammals, J. Appl. Physiol. **22**, 453 (1967).

[47] A. Kepecs, N. Uchida, and Z. F. Mainen, Rapid and precise control of sniffing during olfactory discrimination in rats, J. Neurophysiol. **98**, 205 (2007).

[48] S. L. Youngentob, M. M. Mozell, P. R. Sheehe, and D. E. Hornung, A quantitative analysis of sniffing strategies in rats performing odor detection tasks, Physiol. Behav. **41**, 59 (1987).

[49] D. W. Wesson, T. N. Donahou, M. O. Johnson, and M. Wachowiak, Sniffing behavior of mice during performance in odor-guided tasks, Chem. Senses **33**, 581 (2008).

[50] J. V. Verhagen, D. W. Wesson, T. I. Netoff, J. A. White, and M. Wachowiak, Sniffing controls an adaptive filter of sensory input to the olfactory bulb, Nat. Neurosci. **10**, 631 (2007).

[51] M. J. Tobin, M. J. Mador, S. M. Guenther, R. F. Lodato, and M. A. Sackner, Variability of resting respiratory drive and timing in healthy subjects, J. Appl. Physiol. **65**, 309 (1988).

[52] G. Benchetrit, Breathing pattern in humans: Diversity and individuality, Respir. Physiol. **122**, 123 (2000).

[53] R. Hämäläinen and A. Viljanen, Modelling the respiratory airflow pattern by optimization criteria, Biol. Cybernetics **29**, 143 (1978).

[54] N. Sobel, R. M. Khan, C. A. Hartley, E. V. Sullivan, and J. D. Gabrieli, Sniffing longer rather than stronger to maintain olfactory detection threshold, Chem. Senses **25**, 1 (2000).